Emergent functionalities enhanced by mechanical stress in SnO_2-based flexible devices

Makoto Sakurai
International center for Materials Nanoarchitectonics (MANA), National Institute for Materials Science (NIMS), 1-1 Namiki, Tsukuba, 305-0044, Japan

Email: sakurai.makoto@nims.go.jp

Received xxxxxx
Accepted for publication xxxxxx
Published xxxxxx

Abstract

Emergent functionalities created by applying mechanical stress to flexible devices using SnO_2 microrods and Ga_2O_3/SnO_2-core/shell microribbons are reviewed. Dynamic lattice defect engineering through application of mechanical stress and a voltage to the SnO_2 microrod device leads to a reversible semiconductor-insulator transition through lattice defect creation and healing, providing an effective and simple solution to the persistent photoconductivity (PPC) problem that has long plagued UV semiconductor photosensors. Here, lattice defects are created near slip planes in a rutile-structured microrod by applying mechanical stress and are healed by Joule heating by applying a voltage to the microrod. Nanoscale amorphous structuring makes the Ga_2O_3/SnO_2-core/shell microribbon with a large SnO_2 surface area more sensitive to changes in temperature, while mechanical bending of the wet device improves its sensitivity to adsorbed water molecules. These results illustrate the potential for developing flexible devices with new functionalities by enhancing the intrinsic properties of materials through miniaturization, mechanical stress, and hybridization.

Keywords: SnO_2, Ga_2O_3, mechanical stress, rutile structure, defect engineering, humid sensor

Color printing only online

1. Introduction

Material nanoarchitectonics is a new path for the development of devices from new materials. It goes beyond the mere creation of nanomaterials to include new functionalities developed through the understanding and control of interactions between individual nanostructures and the integration of nanostructures [1]. This paper provides a comprehensive review of this concept and new functionalities, such as reversible control of lattice defects, as well as enhancement of sensing functionalities through nano- and microstructured metal oxides such as SnO_2 and Ga_2O_3.

Lattice defects in oxides and semiconductors alter the optical, electrical, and magnetic properties of materials. In contrast to methods that control lattice defects by healing defects in crystals through thermal annealing [2-4] or by growing crystals from materials mixed with small amounts of impurities [5-7], the method used in these studies dynamically creates and heals lattice defects [8]. This is a kind of lattice

defect engineering by applying mechanical stress and voltage. The SnO_2 used in these studies is a wide bandgap oxide material, with a bandgap of 3.6 eV [9, 10]. The reason for choosing it is that SnO_2 crystals have a rutile structure. The rutile structure has inversion symmetry and does not produce a piezoelectric field effect. Thus, the changes in the properties caused by bending the crystal can be directly measured and analyzed without having to consider the effect. In the case of single crystals, it is known that their structures are elastically deformed by applying a small external mechanical stress [11]. When the deformation is below the elastic limit, the crystal returns to its original shape when the stress is removed. On the other hand, bending above the elastic limit causes plastic deformation; the crystal does not return to its original state even when the stress is removed (figure 1(a)). To control the creation and healing of lattice defects, sliding of split planes in rutile-structured SnO_2 microrods can be exploited by applying mechanical stress [12,13] and through Joule heating generated by applying a voltage [8,13]. In the case of amorphous and polycrystalline nano-/microstructures, deformation caused by applying mechanical stress induces gaps and expands the grain boundary, leading to an increase in surface area. This mechanical stress induced change in surface area can be exploited in order to enhance the sensing capability of Ga_2O_3/SnO_2 core-shell devices [14, 15]. A SnO_2-based device was fabricated on a flexible substrate (figure 1(b)) and bent by applying stress from the back of the substrate (figure 1(c)). Electrodes on both sides of the rod were used to measure the change in electrical resistance during bending and to apply a voltage to generate Joule heating for electrical healing. The strain ε of the sample was obtained from the bending of the substrate by using the following simple equation (figure 1(c)):

$$\varepsilon = \frac{t_{\text{polymer}} + t_{\text{sample}}}{2R_c}, \qquad (1)$$

where $\boldsymbol{t_{\text{polymer}}}$ is the thickness of the polymer sheet, $\boldsymbol{t_{\text{sample}}}$ is the thickness of the sample, and the denominator approximates a bend with the radius of curvature R_c. Section 2 discusses reversible control of lattice defects and the solution to the persistent photocurrent (PPC) effect by using SnO_2 microrod devices, and Section 3 focuses on the sensitivity of Ga_2O_3/SnO_2-core/shell microribbon devices and its enhancement by applying mechanical stress.

2. Emergent functionalities in SnO_2 microrod devices

2.1 Preparation and structure of SnO_2 nano/microrods

SnO_2 nano/microrods were prepared by vapor phase growth in an electric furnace, and their morphology and structure were

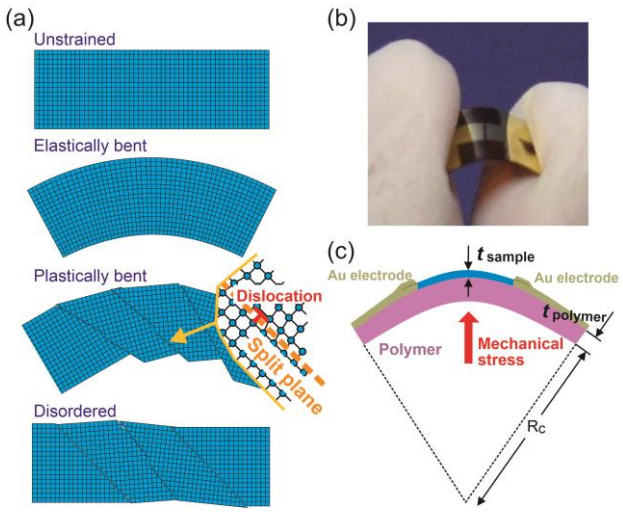

Figure 1. (a) Schematic states of bent single-crystal rod with rutile-structure studied in this review. Slip planes form when the rod is bent beyond its elastic deformation limit. (b) Photograph of wire device bent by mechanical force. (c) Strain (ε) of the rod as determined from the polar radius R_c, thickness of the polymer substrate (t_{polymer}) and sample (t_{sample}), as in Equation (1).

investigated. A mixture of SnO_2 powder and carbon powder in a mass ratio of 1:1 was placed in an Al_2O_3 boat. The furnace was heated to about 473 K to evaporate water and extra gases contained in the boat and the quartz tube of the furnace for about 10 minutes. Then, the furnace temperature was raised to 1263 K, and the reduction reaction between SnO_2 and carbon was continued for about 60 minutes in high-purity argon carrier gas (9×10^2 Pa) mixed with 4% oxygen gas. The vapor of Sn atoms was carried by a carrier gas to grow the nano/microrods. The SnO_2 microrods had a prismatic structure with a square cross-section of about 2 μm on one side (figure 2(a)) and a length of 3 - 5 mm [8]. The microrods grew from tiny SnO_2 crystal nuclei which were formed by the high-density atomic Sn gas on the surface of the Al_2O_3 boat (figure 2(b)). The SnO_2 nanorods were formed by the catalytic reaction of gold particles on the sapphire (001) substrate [12]. The TEM image and diffraction pattern of the SnO_2 nanorod show the growth in the [001] direction (figure 2(d)).

The structure of a single SnO_2 microrod was investigated by making X-ray diffraction measurements (figure 2(c)) [16]. Peaks corresponding to the (002), (004), and (006) orientations of the SnO_2 crystal were observed when the scattering vector $\boldsymbol{q}$ was oriented in the axial direction of the microrod, and peaks in the (200), (400), and (600) orientations of the structure were observed when $\boldsymbol{q}$ was taken diagonally across the square cross-section of the microrod. The lattice constants of this single crystal were a = 0.478 nm and c = 0.318 nm. It was confirmed that the single crystal had a rutile structure and that the (110) plane was one side of the prism

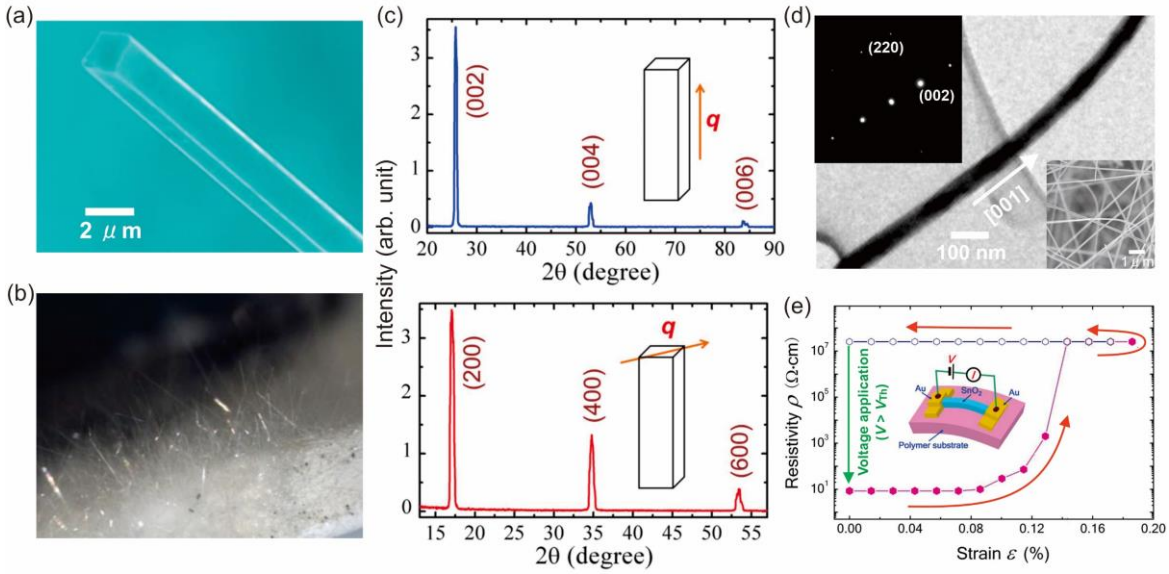

Figure 2. (a) Scanning electron microscope (SEM) image of as-grown single-crystal SnO_2 microrod. (b) Optical microscope image of as-grown SnO_2 microrods grown on the edge of an Al_2O_3 boat. (c) XRD pattern of as-grown SnO_2 microrod: scattering vector *q* parallel to rod axis, scattering vector *q* parallel to the diagonal line of square cross-section of SnO_2 microrod [16]. (d) TEM image of single SnO_2 nanorod. Upper inset: TEM diffraction pattern of nanorod near the edge of the supporting carbon sheet. Lower inset: SEM image of as-grown SnO_2 nanorods. (e) Resistivity of SnO_2 microrod device as a function of mechanical strain at V =2.0 V. The strain is increased from 0 to 0.186% (pink hexagons) and then decreased to 0 (blue open hexagons). The resistivity returns to its original value when the applied voltage is above the threshold voltage V_{Th}. The inset shows a schematic illustration of the bent SnO_2 device [8].

[16]. Transmission electron microscopy diffraction images of SnO_2 nanowires confirmed that they also had a rutile structure with the same crystallographic orientation as the microrods (figure 2(c))[12].

2.2 Electrical properties of a bent SnO_2 microrod

The electrical properties of a single crystal SnO_2 microrod were investigated at 297 K (figure 2(e)). A SnO_2 microrod was placed on a flexible polyimide sheet with a thickness of 0.125 mm, and gold electrodes were deposited on both ends of the rod to fix it to the sheet. The resistance was measured by applying a voltage between the electrodes spaced 200 μm apart. SnO_2 becomes an n-type semiconductor due to intrinsic impurities such as oxygen defects [10], and the resistivity of the SnO_2 microrods was about 10 Ωcm at 297 K. This state is called the semiconducting state.

The resistivity change was measured at 297 K and an applied voltage of 2 V by bending the SnO_2 microrod device by applying stress from the back of the polyimide sheet (figure 1(c)) [8]. The resistance of the bent microrod is plotted as a function of the strain ε in figure 2(e). In the low strain region ($\varepsilon \leqq 0.12\%$), the resistivity changed reversibly. When the strain was removed, the resistivity returned to its original value, indicating that the microrod was elastically deformed. When the strain was further increased, the resistivity did not return to its original value even after the stress was removed. This indicates that irreversible lattice defects were created in the microrod; i.e., plastic deformation beyond the critical limit of elastic deformation occurred (figure 1(a)). When the strain was increased further, the resistance reached the limit of the measurement system (~2×10^7 Ωcm). This state is called the insulating state. When the strain was reduced to zero, the device remained in the insulating state (figure 2(e)). When a voltage of 6.5 V or higher was applied to the device in the insulating state, the resistivity returned to its original value [8]. Thus, the transition from the semiconductor state to the insulating state due to mechanical stress in the microrod device had nonvolatile characteristics. This means that the transition between the semiconducting and insulating states can be controlled by applying mechanical stress and voltage.

2.3 Structural analysis of a bent SnO_2 nano/microrod

The structural changes in a bent SnO_2 microrod were investigated by micro-Raman spectroscopy at 297 K to confirm that the transition from the semiconducting state to the insulating state under mechanical stress is due to lattice defects created in the microrod. Two peaks at 631 cm^{-1} and 733 cm^{-1} appeared in the Raman spectra of a SnO_2 microrod in the semiconducting state ($\varepsilon = 0$) before bending (figure 3(a)), corresponding to the $A1_g$ and $B2_g$ modes, respectively [17,18]. No peaks corresponding to the E_g mode appeared. On the other hand, peaks corresponding to the E_g mode appeared in the spectrum of the microrod in the insulating state produced by

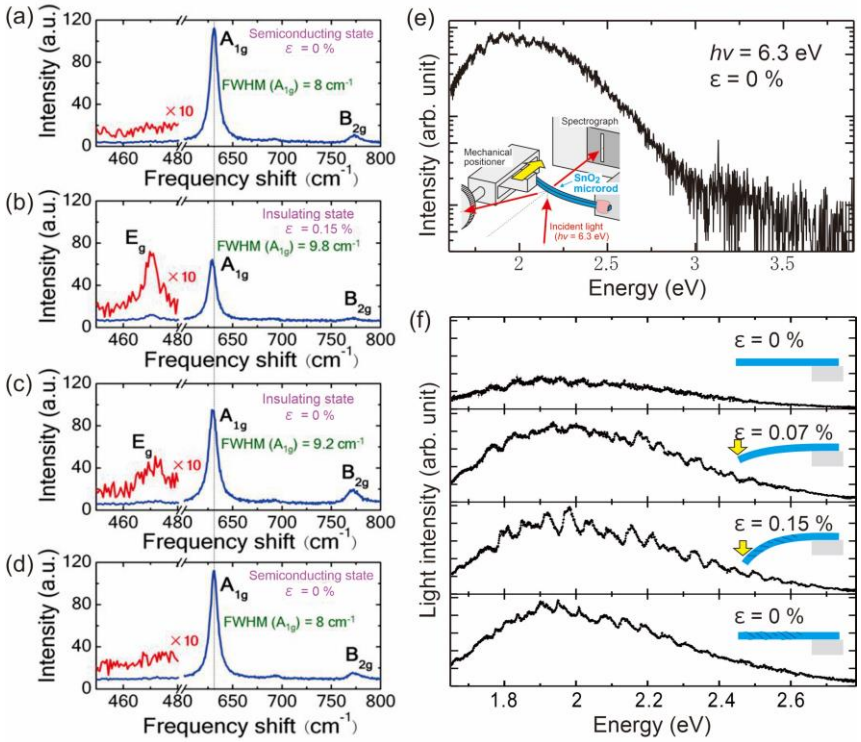

Figure 3. Micro-Raman spectra of SnO_2 microrod at 300 K under different strain conditions. The vertical dotted line shows the peak of the A_{1g} mode at $\varepsilon = 0$. (a) Original straight SnO_2 microrod in the semiconducting state (strain $\varepsilon = 0$). (b) Bent SnO_2 microrod in the insulating state ($\varepsilon = 0.15$ %). (c) Microrod in the insulating state after straightening (ε = 0). (d) Microrod in the semiconducting state by applying a voltage across the microrod ($\varepsilon = 0$) [8]. (e) PL spectrum of as-grown single SnO_2 microrod at 300 K [12]. Inset: Schematic experimental setup of the PL experiment where mechanical stress is applied to the SnO_2 microrod. (f) PL spectra of SnO_2 microrod with one end fixed and mechanical stress applied to the other end at 300 K [12].

bending (ε = 0.15%) (figure 3(b)) and the $A1_g$ peak position shifted to the lower wavelength side. The half-value width of the $A1_g$ peak was broadened. The appearance of the E_g mode indicates the presence of a region with a tilted crystal orientation. The shift in the peak position is due to the presence of tensor stress along the c-axis [19], and the increase in the peak width is due to the reduced crystallinity of the microrod. These spectral changes remained in the insulating state of the microrod after the strain was removed (figure 3(c)), indicating that lattice defects remained in the microrod. When a voltage of more than 6.5 V was applied to the device, the spectrum returned to its original state (figure 3(d)), and the crystallinity was restored.

Since electrons accelerated by high voltage (200 kV) in a transmission electron microscope (TEM) cannot penetrate a SnO_2 microrod with a thickness of about 2 μm, a thin SnO_2 nanorod with a thickness of about 100 nm was used to study the internal structural changes by bending the nanowire [12]. The bending of the nanorod on a TEM grid under the observation of a scanning electron microscope was performed using focused tungsten (W) deposition, a focused gallium (Ga) ion beam, and a sharp needle manipulator equipped with a focused ion beam (FIB) microscope. A small number of SnO_2 nanorods dispersed in organic solvent were dropped onto the TEM grid and an isolated nanorod was used in the bending procedure schematically shown in figure 4(a). One end of the nanorod was fixed to the grid by using focused W deposition (inset 1 in figure 4(a)). The needle was brought into contact with the other end and attached to it by the deposited W (inset 2). The needle was moved in order to bend the nanorod (inset 3) and was fixed to the grid by the deposited W. The fixed needle was cut off by the focused Ga ion beam irradiation (inset 4). A strain of about 3% was generated in the outer part of the bent nanorod (figure 4(b)). It is important not to irradiate the SnO_2 nanorod with the beam because the beam would easily create many defects and lose crystallinity.

The TEM images of the bent SnO_2 nanorod showed unique features resulting from plastic deformation of a rutile crystal. In the bent nanorod, black stripes appeared that were inclined at about 45° to the direction of rod growth (see the arrows in figure 4(c)). A step-like structure appeared in a magnified TEM image of the outside of the bent nanorod (Figure 4(d)). On the other hand, the surface of the unbent nanorod was almost smooth (figure 4(e)). Slip planes along the $(10\bar{1})$ plane in a rutile crystal [20, 21,22] were created by bending the nanorod. A step-like structure, shown schematically in figure 4(f), was caused by the slip plane. Lattice defects such as oxygen vacancies were generated near these planes and appeared as black stripes in the TEM image (figure 4(c)). In addition, a dislocation appeared in a magnified TEM image of this region (figure 4(g)). It was concluded that the plastic deformation resulting from slip planes forming could occur in a bent SnO_2 microrod with the same crystal structure. In addition, charge carriers were trapped at the oxygen vacancies

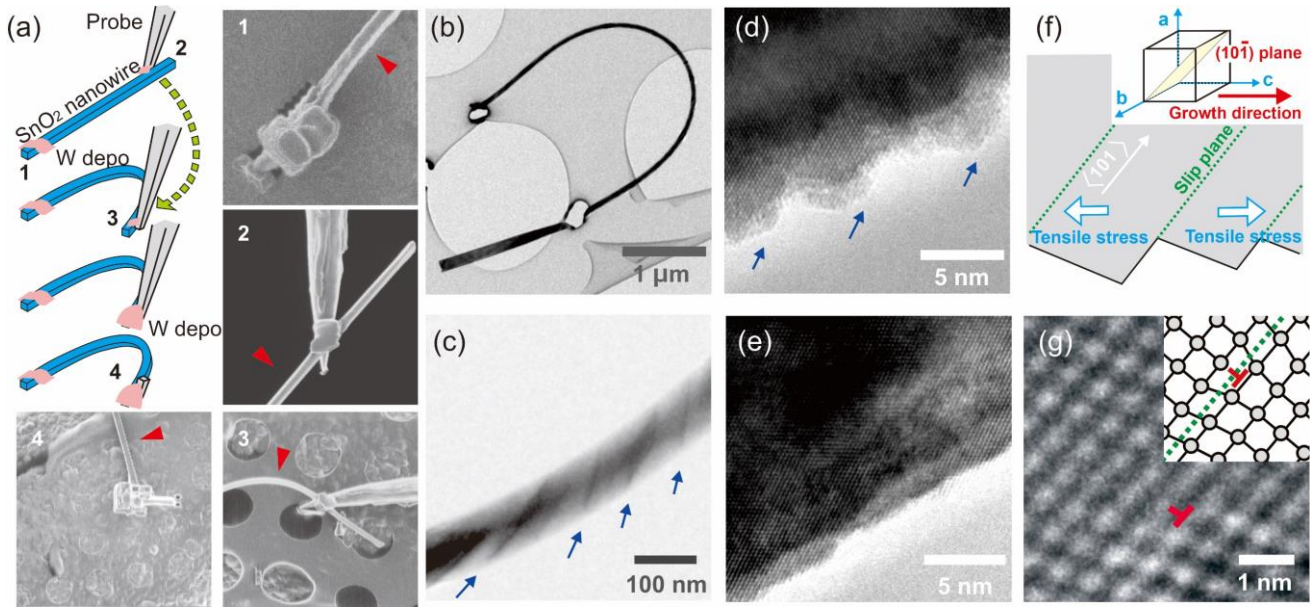

Figure 4. (a) Schematic diagram showing the fabrication of a bent nanowire using a sharp metal probe and focused tungsten deposition in a FIB machine. The insets are scanning electron microscope images of a SnO_2 nanowire bending by the FIB method. The red arrow indicates the SnO_2 nanowire. The number in the inset corresponds to the area numbered in the schematic diagram. (b) TEM image of bent single-crystal SnO_2 nanowire on a thin carbon support layer of a TEM grid. (c) TEM image of bent single-crystal SnO_2 nanowire under 3% strain. Black stripes with blue arrows indicate the formation of slip planes in the rutile structure. (d) High-magnification TEM image of the outer surface under tensile strain. Arrows indicate step-like surface structures. (e) High-magnification TEM image of the outer surface of an unbent SnO_2 nanowire. (f) Schematic diagram showing slip planes formed by tensile strain. The inset shows the geometric relationship between the [001] growth direction and the $(10\bar{1})$ plane in the rutile structure. (g) High-magnification TEM image of a SnO_2 nanowire with dislocations under tensile strain. The inset schematically shows the dislocation at the slip plane [12,13].

created near the slip plane, resulting in an increase in electrical resistance (figure 2(c)).

2.4 Change in electronic state of a bent SnO_2 microrod

The electronic state of a bent SnO_2 microrod at 297 K was studied by using the photoluminescence (PL) method to see how the electronic state of the microrod changed by bending. One end of the microrod was fixed and mechanical stress was applied to the other end with a mechanical positioner (inset of figure 3(e)). The bent microrod was irradiated with laser light ($h\nu$ = 6.3 eV), and the light emitted from the microrod was detected by using a spectrograph and a CCD camera. The PL spectrum of the unbent microrod (ε = 0) at 297 K showed no peak at 3.6 eV due to direct electron-hole recombination across the energy bandgap (figure 3(e)). This is because carriers excited to the conduction band by the irradiation decay to shallow donor levels located 0.03 - 0.15 eV below the bottom of the conduction band, followed by an optical transition to energy levels due to oxygen defects in the band gap [17]. Thus, the PL spectrum of the unbent microrod showed a broad peak centered at energies of 1.9 - 2.3 eV (figure 3(e)). The peak intensity increased by bending the microrod (figure 3(f)). This was due to the formation of lattice defects such as oxygen vacancies near the slip planes (figure 4), which increase the density of energy levels in the band gap [17,18] and cause an increase in the optical transitions of photo-excited electrons to these levels. The intensity changed little after the stress was removed. These results demonstrate the non-volatile nature of the mechanically induced lattice defects in the microrod.

2.5 Electric healing of a lattice defect in a SnO_2 microrod

Electrical healing of lattice defects in the microrod was experimentally investigated to understand how defects are healed by the applying voltage between the ends of the microrod. The creation and healing processes depended on the voltage (figure 5(a)). When more than 4 V was applied, the insulator-semiconductor transition occurred before the strain reached zero. As the voltage was increased, the threshold strain of the semiconducting-to-insulating transition increased. The threshold strains in the transition are plotted as a function of the applied voltage in figure 5(b). The increase in both strains with voltage indicates that the current flowing in the microrod caused the lattice to heal electrically, analogously to the annealing of defects by Joule heating.

The time-dependent response to an applied pulse voltage in the microrod device was used to elucidate the mechanism behind the electrical healing [13]. The current change in

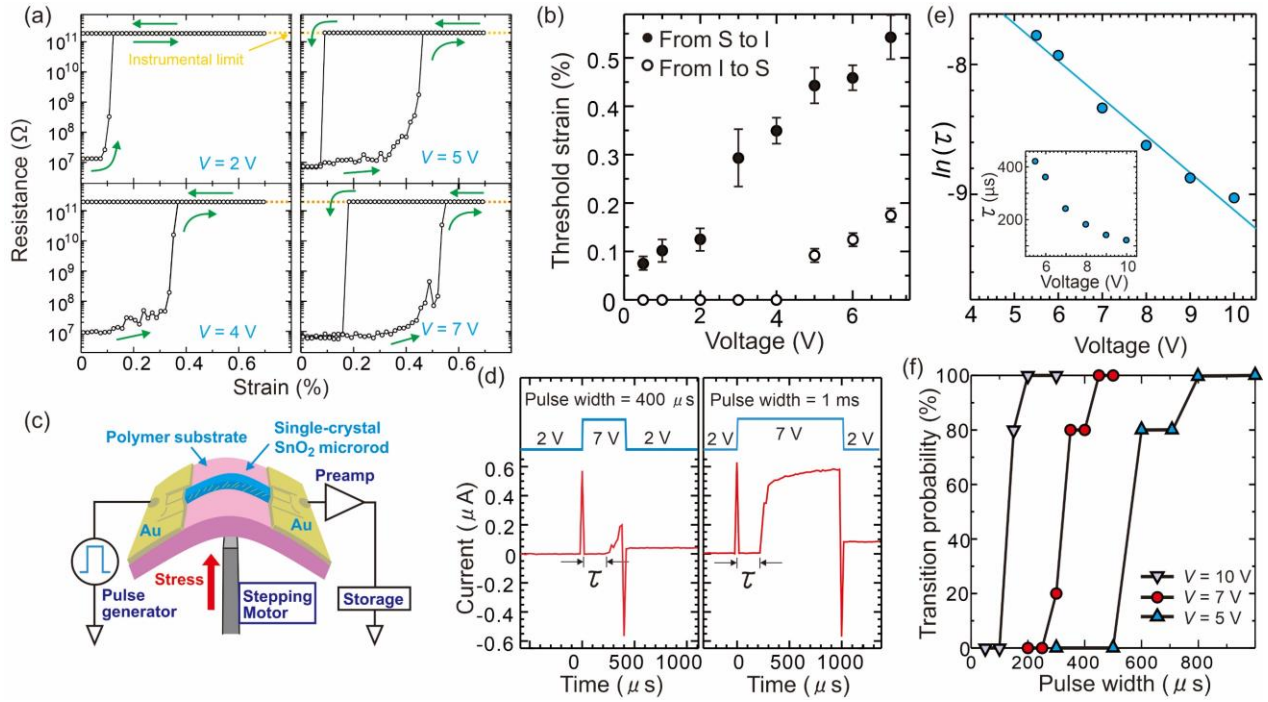

Figure 5. (a) Strain versus resistance curves for the SnO2 microrod device at V_b = 2, 4, 5, and 7 V and T = 300 K. (b) Threshold strain at semiconducting-to-insulating transitions (closed circles) and insulating-to-semiconducting transitions (open circles) versus voltage applied between the electrodes. (c) Schematic illustration of dynamic measurement of SnO_2 microrod devices under application of mechanical stress and pulse voltage. The distance between the Au electrodes is 120 μm for a single-crystal SnO_2 microrod. (d) Change in current of the device in the insulating state after a time delay τ in response to pulse voltage (V = 7 V and pulse width of 400 μs and 1 ms). (e) The logarithm of τ is linearly related to the applied voltage. Inset: Time delay τ of the response of SnO_2 microrod devices in the insulating state to each pulse voltage at T = 300 K. (f) Probability of transition from the insulating to the semiconducting state in the microrod device as a function of pulse width for V = 5, 7, and 10 V at T = 300 K [12,13].

response to the pulsed voltage was converted by a current-voltage preamplifier, and the voltage change was monitored on a storage oscilloscope (figure 5(c)). The SnO_2 microrod device was first bent to produce an insulating state and then returned to zero strain to produce an unbent microrod in the insulating state. A 7-V pulse voltage was applied to the device for 400 μs and 1 ms (figure 5(d)). A spike current signal appeared when the pulse was applied. This signal is due to accumulation of charge on the metal electrodes, similar to the accumulation of charge in a capacitor. The current began to flow after a time τ, and the current increase became slower with the passage of time, suggesting different electrical healing processes before and after the current flow. After applying the 7-V pulse voltage, the voltage was changed to 2 V. The amount of charge stored in the metal electrodes decreased and excess charge began to flow, causing a spike-like negative current to flow. After applying the pulsed voltage for 1 ms, a current of about 0.1 μA flowed through the device, indicating that the microrod had changed to the semiconducting state.

Electrical healing before the current flow was examined. The time τ from the onset of the pulse voltage to the onset of the current flow decreased as the applied voltage increased (inset in figure 5(e)). A plot of the logarithm of τ versus voltage V showed a linear relationship (figure 5(e)), indicating that carriers trapped by the potential at defect sites such as oxygen vacancies were released by the reduction of the barrier. The mechanism of trapping and release of carriers by the potential barrier is similar to the Poole-Frenkel effect [19], indicating that τ is proportional to the probability that the carriers overcome the voltage-reduced trapping barrier by thermal activation.

The electrical healing that occurs after the current flow is due to Joule heating. The transition from the insulating to the semiconducting state depends on the pulse voltage value and the pulse width (figure 5(f)) and requires a long pulse width for a small voltage pulse. Defect healing is the rearrangement of atoms into a regular order by migration of atoms and defects [2-4]. This local recrystallization requires energy, which is provided by the Joule heating generated by the applied voltage. The gradual increase in current when the pulsed voltage is

being applied (figure 5(d)) indicates that the defects are slowly healed by the Joule heating. It is important to note that in this case, lattice defects such as oxygen defects form along the slip planes. Since crystal plane migration along the planes occurs with less damage to the crystal, and since oxygen gas tends to migrate along these plane boundaries [9], the energetic barrier to defect healing in the SnO_2 microrod is low, and the lattice defects can be healed by applying a voltage for a short time. This healing process is quite different from that of an oxide nanowire with large mechanically created defects where a depressed defect region created by pressing a sharp probe on an oxide nanowire is partially healed by prolonged application of Joule heating to the nanowire [23].

2.6 UV photo sensitivity of a SnO_2 microrod device

SnO_2 is a wide bandgap material (E_g = 3.6 eV), in which ultraviolet (UV) light excites carriers in the valence band to the conduction band across the bandgap and the measurement of the photo-induced carriers works as a monitor of the UV light, indicating that SnO_2 works as a semiconductor UV photosensor. The photo-induced current I_{photo} was measured by changing the wavelength of the light irradiating the SnO_2 microrod (figure 6(a)) [16]. The optical response R_λ was calculated as $R_\lambda = I_{photo}/SP_\lambda$, where S is the light-exposed area and P_λ is the wavelength-dependent intensity of the incident light. The plot of R_λ versus wavelength λ (figure 6(a)) shows that R_λ increases rapidly below a wavelength close to the bandgap energy (~345 nm) of SnO_2. The relationship between the optical response R_λ and the internal gain G in the material is as follows [24]:

$$R_\lambda = \frac{q\lambda\eta G}{hc}, \qquad (2)$$

where q is the fundamental charge, λ is the wavelength, η is the quantum efficiency, h is Planck's constant, and c is the speed of light. R_λ of the SnO_2 microrod device at 250 nm is ~3 × 10^8 A/W. Assuming a quantum efficiency η of 100% and using equation (2), the internal gain G would be ~1.5 × 10^9. This is one to two orders of magnitude larger than G (10^6 - 10^7) of conventional SnO_2 nanowire photosensors [25-27].

2.7 Solving the PPC problem by controlling lattice defects in a SnO_2 microrod device

Lattice defect engineering in SnO_2 microrod devices was used to solve the PPC problem [28] that has affected UV semiconductor sensors; that is, when these devices are irradiated with UV light (260 nm), the photo-induced current increases rapidly in a short time (figure 6(b)). Irradiation experiments were performed under three different conditions (296 K air, 331 K air, and 296 K vacuum). When the light

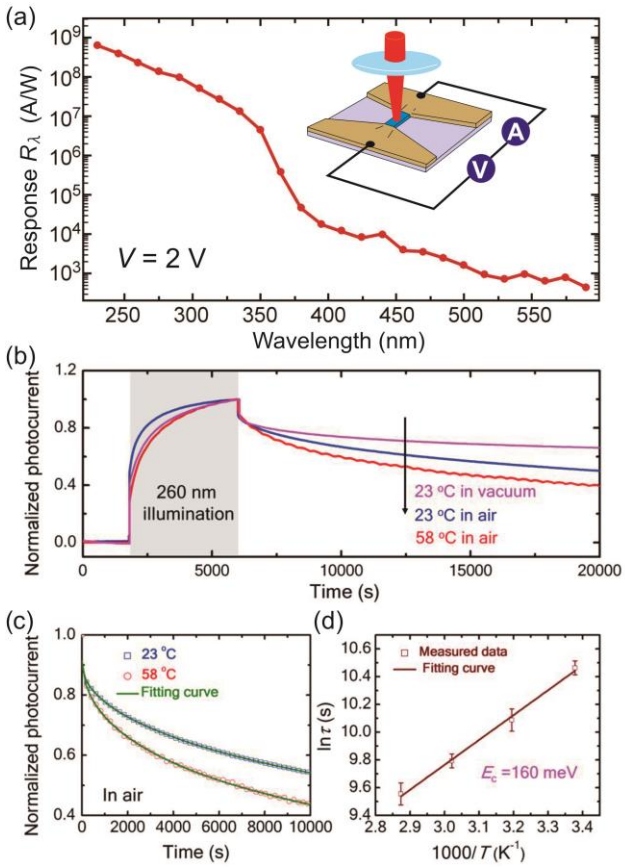

Figure 6. (a) Photoresponse spectrum of SnO_2 single microrod photosensor at 296 K for an applied voltage of 2 V. The inset shows the schematic experimental setup. (b) Typical PPC behavior in SnO_2 single microrod irradiated by 260 nm UV light at 2 V applied voltage under different conditions: 296 K in vacuum, 296 K in air and 331 K in air. The excitation intensity is about 0.05 μW/cm^2. (c) Normalized photocurrent decay in air at 296 K (open squares) and 331 K (open circles). The PPC decay time constants are determined by fitting the decay curves with the stretched-exponential equation. (d) Arrhenius plot of PPC decay time constant as a function of inverse temperature [16].

irradiation was stopped, the photo-induced current decayed slowly. The decay at 296 K in air was faster than that in vacuum. This is because devices in a vacuum have more oxygen vacancies on the surface and inside, suggesting that carrier trapping by oxygen vacancies is the cause of the PPC problem [29]. The carrier trapping energy in the PPC problem was elucidated by analyzing the decay curves of devices at different temperatures in air. The PPC decay can be described by an extended exponential function [28]:

$$I_{PPC}(t) = I_{PPC}(0)\exp\left[-(t/\tau)^\beta\right] \qquad (3)$$

where I_{PPC} (0) is the current immediately after the light irradiation is stopped, τ is the time constant of the PPC decay, and β is the exponential factor of the decay ($0 < \beta < 1$). τ and β were determined from the best fit of equation (3) to the data

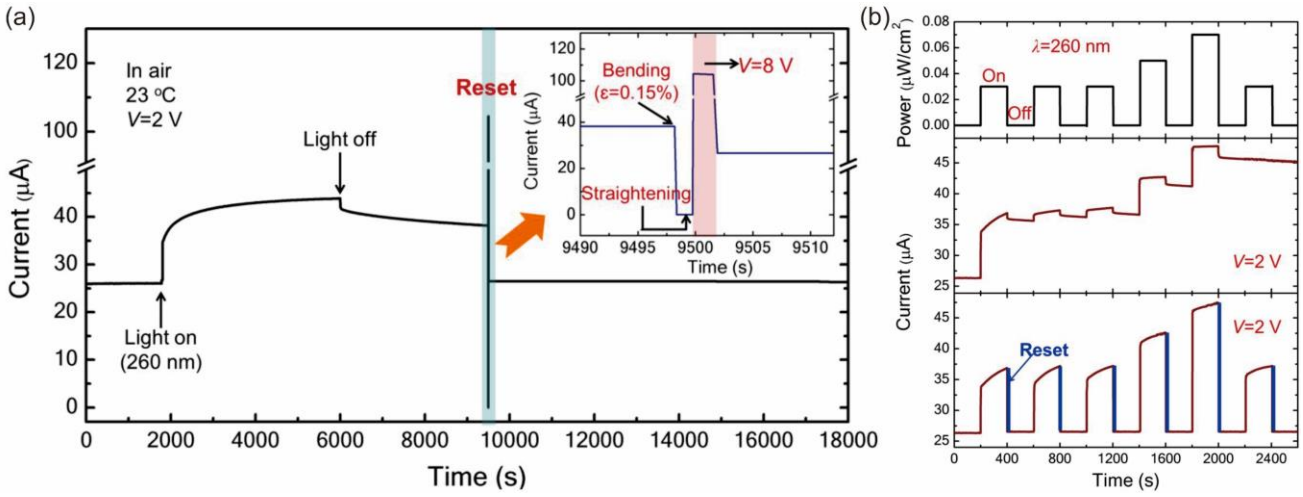

Figure 7. (a) Photoresponse spectrum of SnO_2 single microrod photosensor at 296 K for an applied voltage of 2 V. (b) Time-dependent photocurrent response measured in dry air at a bias voltage of 2 V under 260-nm illuminations with different intensities. Good reproducibility is obtained after the reset process [16].

(figure 6(c)). β ranged from 0.51 to 0.54. Plotting the logarithm of τ for each temperature against the reciprocal of the temperature yielded a linear relationship (figure 6(d)), suggesting that the time constant of the decay is determined by a thermal activation process. This process can be expressed by the following equation [28]:

$$\tau(T) = \tau_0 \exp\left[E_C/k_B T\right], \qquad (4)$$

where E_C is the carrier trapping potential and τ_0 is a constant that determines the time scale. From the slope of the line obtained from the experimental data, E_c is required to be 160 meV (figure 6(d)). This means that the PPC problem is caused by photo-excited carriers becoming trapped by an energy barrier of 160 meV at the oxygen vacancies.

The PPC problem was solved by exploiting the lattice defect engineering method used in the SnO_2 microrod devices. A photocurrent was induced by irradiating the devices with UV light (260 nm) in air at 296 K (figure 7(a)). After the light irradiation was stopped and the PPC decay of the current began to occur, a reset process was applied to the device (inset in figure 7(a)); the device was bent (ε = 0.15%) to bring it into the insulating state and then it was unbent (ε = 0%). A voltage of 8 V was then applied to the device for 2 seconds for electrical healing. After applying this reset process, the photo-induced current decreased rapidly and returned to its original value (figure 7(a)). Thus, the lattice defects created near the generated slip planes acted as recombination centers for photoexcited electron-hole pairs, and the Joule heating generated for the electrical healing released carriers trapped at the defect sites and promoted the transition to the ground state by recombination. Continuous pulsed UV light (260 nm) irradiation of the microrod device (top panel in figure 7(b)) reduced the signal-to-noise (SN) ratio of the photoinduced current response due to the PPC problem (middle panel). On the other hand, when the reset process was applied immediately after the pulsed UV irradiation, the photocurrent showed a good response with a high SN ratio (bottom panel). Thus, the reset process using lattice defect engineering proved to be an effective solution to the PPC problem of semiconductor UV photosensors.

3. Emergent sensitivity in hybrid SnO_2-based devices

SnO_2 materials are widely used as commercial gas sensors and exhibit good sensitivity to relative humidity (RH) at low temperatures [9,10]. However, the described SnO_2 microrod device did not function as a gas sensor (lower inset in figure 9(a)) because its electrical properties did not change when water molecules adsorbed on the surface under high RH conditions. This was due to the small surface-to-volume ratio. The current was dominated by the flow inside of the microrod. This section describes functionalized SnO_2-based devices as an example of using material nanoarchitectonics to overcome this weakness. In particular, to show the potential of material nanoarchitectonics, Ga_2O_3, which has a large bandgap (4.7 eV) and a polymorphic nature, was hybridized with SnO_2. In addition, mechanical stress was applied to the hybridized device as a way to activate its functionality.

3.1 Preparation and characterization of microribbons composed of SnO_2 and Ga_2O_3

The hybrid structure was formed in a one-step fabrication using vapor phase growth of SnO_2 and Ga_2O_3 [14]. Since Ga_2O_3 has a higher melting point than SnO_2, there is a

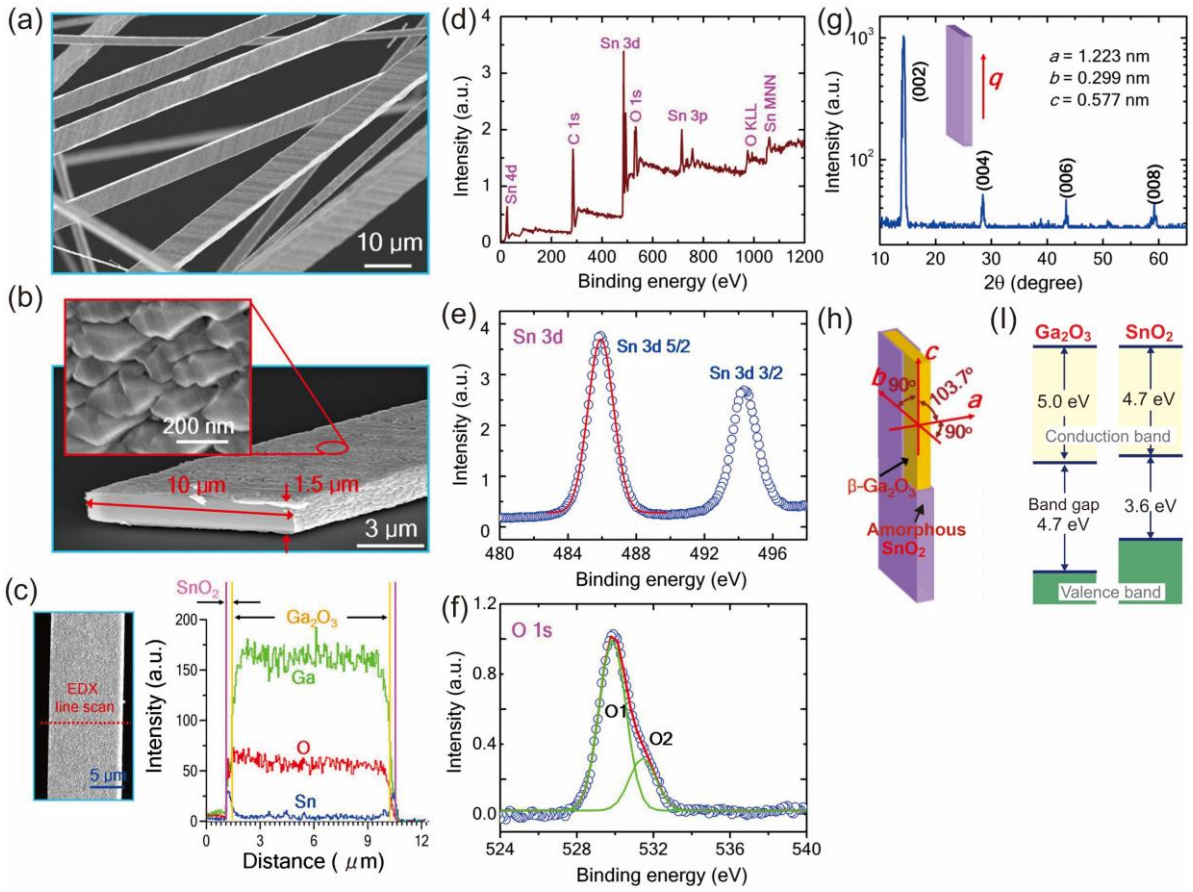

Figure 8. SEM images of as-grown β-Ga_2O_3/amorphous-SnO_2 core/shell microribbons at (a) low and (b) high magnifications. (c) SEM image of microribbon and EDX line scanning profiles of Ga, O, Sn components in core/shell microribbon. XPS spectra showing binding energy of (d) all, (e) Sn, and (f) O atoms. The Sn 3d 5/2 peak shows a symmetric component without shoulders (Red curve: Gausian fitting). (g) XRD patterns of as-grown single microribbon with the scattering vector ***q*** parallel to the rod axis [14]. (h) Schematic structure of a Ga_2O_3/ SnO_2 core/shell microribbon. (i) Schematic energy band diagram of Ga_2O_3 and SnO_2.

difference in the temperature at which the respective atomic gases aggregate and crystallize. This difference was exploited to create a hybrid structure. A mixture of SnO_2, Ga_2O_3, and carbon powder in a mass ratio of 1:1:2 was placed in an Al_2O_3 boat, and vapor phase growth was performed in an electric furnace at 990 °C by using argon gas (9×10^2 Pa) mixed with 4% oxygen as a carrier gas. A Ga-based material was first grown as the core of the structure. As the temperature decreased, Sn atomic gas was adsorbed on the surface and formed scaly-like shell structures (figure 8(b)). The microribbon had a rectangular cross-section of about 10 μm × 1.5 μm (Figures 8(b)). The shell was covered with scaly structures with a lateral size of about 200 nm. Local EDX measurements of the microribbon showed that the shell contained Sn atoms with a thickness of about 300 nm (figure 8(c)). Since the XPS spectrum in the energy range of 0-1200 eV shows peaks ascribed to Sn, O, C (figure 8(d)), the ribbon is covered by Sn-based layers. Figure 8(e) shows double spectral lines of Sn 3d at binding energies of 485.9 eV (Sn 3d 5/2) and 494.3 eV (Sn 3d 3/2) with a spin-orbit splitting of 8.4 eV, which is consistent with Sn^{4+} ion bound to oxygen in the SnO_2 matrix [14]. The O 1s peaks are composed of a peak (531.1 eV) of O^{2-} from the rutile structure of SnO_2 and a peak (532.7 eV) of thin hydroxide on the surface of amorphous SnO_2 (figure 8(f)) [14]. There were no peaks corresponding to SnO_2 in the X-ray diffraction pattern of the single microribbon (figure 8(g)), suggesting that the shell was composed of amorphous SnO_2. Analysis of the X-ray diffraction pattern corresponding to the Ga-based core (figure 8(g)) showed that the lattice constant was the same as that of β-Ga_2O_3 among the polymorphic oxide gallium, indicating that the core was composed of a β-Ga_2O_3 single crystal. From these analyses, it was concluded that the microribbon had a β-Ga_2O_3/amorphous SnO_2 core/shell structure (figure 8(h)).

3.2 Ultra-sensitive humidity sensing using Ga_2O_3/SnO_2-core/shell microribbon device

A core/shell microribbon device was fabricated by attaching gold electrodes to both ends of a core/shell microribbon placed on a polyimide sheet [14]. The resistance

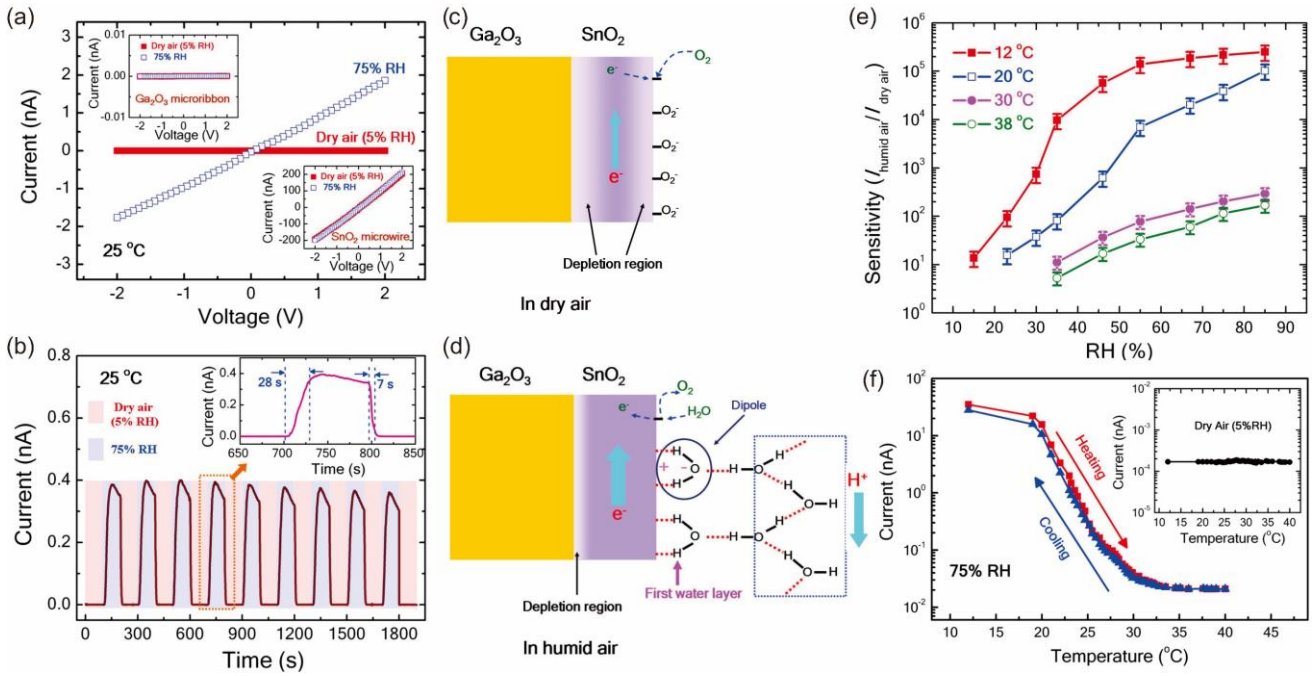

Figure 9. (a) *I-V* curves of core/shell microribbon-based humidity sensor in dry air (5% RH) and 75% RH air at 298 K. The upper and lower insets show the *I-V* curves of Ga_2O_3 microribbon and SnO_2 microwire control samples, respectively. Both control samples have negligible humidity sensing at 298 K. (b) Dynamic response of Ga_2O_3/SnO_2-core/shell microribbon sensor for detection of 75% RH air. The inset shows that the response time and recovery time were ~28 and ~7 s, respectively. Conductivity models of β-Ga_2O_3/amorphous-SnO_2 core/shell microribbon in (c) dry air and (d) humid air. (e) Sensitivity as a function of RH at different operating temperatures: 285 K (red solid square line), 293 K (blue open square line), 303 K (pink solid circle line) and 311 K (green open circle line). (f) Temperature dependence of sensor current in 75% RH air at V = 1 V. The inset shows the temperature dependence of the sensor current in dry air (5% RH) [14].

of the device was 3.5×10^{12} Ω at 296 K, and the current changed significantly in response to the adsorption of water molecules (figure 9(a)). On the other hand, a SnO_2 microrod device showed no change when water molecules adsorbed on the microrod (lower inset). The resistances of the Ga_2O_3 microrod devices with and without water adsorption were below the measurement limit (upper inset). Their hybridization of SnO_2 and Ga_2O_3 through material nanoarchitectonics enabled us to create a new functionality as follows. This section describes humidity sensing using these core-shell devices and elucidates the mechanism behind their high sensitivity and high response speed.

When the Ga_2O_3/SnO_2-core/shell device was placed in an atmosphere in which the relative humidity (RH) was repeatedly changed between 75% and 5% at 296 K, the current in the device responded reproducibly and rapidly to the humidity change (figure 9(b)). The response time, which is defined here as the time required to reach 90% RH of the saturation value of the current change, was about 28 seconds at high humidity and about 7 seconds at low humidity (inset in figure 9(b)). These response times are shorter than those of conventional humidity sensors [30-33]. The mechanism behind the fast response time of the core-shell device is as follows. The shell in dry air is covered with molecular oxygen ions (figure 9(c)). Most of the carriers in the shell are trapped by these ions adsorbed on the SnO_2 surface and at the boundaries of the nanostructured shell, while some of the carriers in the SnO_2 shell move into the Ga_2O_3 core due to the difference between the Fermi surfaces (figure 8(i)). This causes carrier depletion in the SnO_2 layer and low current flow. In the case of the SnO_2 shell at 75% RH, on the other hand, the oxygen molecular ions on the surface are replaced by water molecules. The charge carriers trapped by the oxygen molecular ions are released and flow through the SnO_2 layers and H^+ ions also follow along the surface water molecular layer (figure 9(d)) [30-32], resulting in high current. Because trapping and release of charge carriers occurs primarily within the shell as it switches between low and high humidity, the device can respond quickly to changes in humidity.

Next, the current of the core-shell device was measured as RH was varied from 15% to 85% at temperatures of 285, 293, 303, and 311 K. The sensitivity $S = I_{\text{humid air}} / I_{\text{dry air}}$, where $I_{\text{humid air}}$ and $I_{\text{dry air}}$ represent the current of the sample in dry air (5% RH) and humid air, respectively, is plotted against RH in

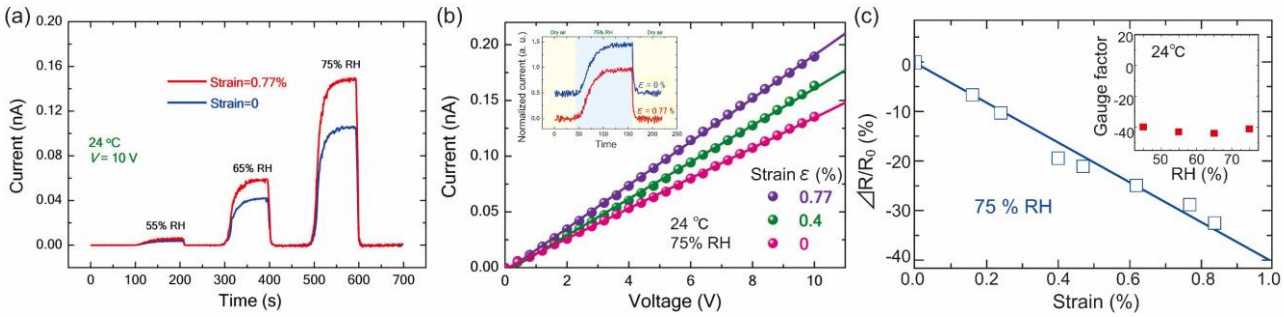

Figure 10. (a) Dynamic response of flexible sensor to different levels of RH under 0 (blue line) and 0.77% strain (red line). The device was operated at 297 K with an applied voltage of 10 V. (b) Linear voltage-current relationship for different strains. The inset shows the time-dependent response at 0% and 0.77 %, respectively. (c) The relative change in resistance ($\Delta R/R_0$) as a function of the tensile strain at 75% RH. The slope corresponds to a GF of -41 [15]. The inset shows GF of the flexible sensor at RH of 45, 55, 65 and 75%.

figure 9(e). As shown, the sensitivity changed by about five orders of magnitude at 285 K under high RH conditions. When the relative humidity was set at 75% RH and the temperature was varied, the current changed by about four orders of magnitude with no hysteresis between the heating and cooling times (figure 9(f)). At 5% RH, however, there was almost no change in current over the temperature range (inset in figure 9(f)). Since $I_{\text{dry air}}$ below 5% RH is on the order of 10^{-4} nA, the humidity sensitivity of core-shell devices is determined by the change in $I_{\text{humid air}}$ due to adsorbed water molecules replacing oxygen ions on the SnO_2 shell. Water adsorption induces the release of electrons from the oxygen ion sites, and the electrons inside the shell and the H^+ ions along the water layers act as a current that is nearly proportional to the number of the water molecules on the shell. When the SnO_2 shell was wet, the device current changed significantly with temperature (figure 9(f)). This temperature-dependent sensitivity is due to the intrinsic nature of SnO_2 materials, namely the physical adsorption property of water molecules on the SnO_2 surface [34]. The molecular partial pressure required for water molecules to adsorb on the SnO_2 surface at a given temperature indicates that water molecules adsorb very easily on the SnO_2 surface at temperatures below 293 K, while adsorption becomes more difficult at temperatures above 293 K. The water adsorptive nature of the microribbon devices indicates the existence of SnO_2 on the shell. The large surface area of the amorphous nanostructured SnO_2 shell makes it possible to access the intrinsic nature of the SnO_2 surface through current measurements as a function of temperature.

3.3 Sensitivity enhanced by bending wet Ga_2O_3/SnO_2-core/shell microribbon device

Bending a core/shell device by applying mechanical stress causes an increase in the humidity sensitivity (figure 10(a)) [15]. The linear current-voltage relationship at 297 K and 75% RH under different strains (figure 10(b)) indicates that the ohmic contact properties between the gold electrode and the device were unchanged by the application of strain. The relative resistance $\Delta R/R_0$, where R_0 is the resistance at zero strain and R_{strain} is the resistance under strain, varied linearly with strain ε (Figure 10(c)). The gauge factor (GF) of the strain is expressed by the following equation:

$$\text{GF} = \frac{\Delta R/R_0}{\varepsilon} = \frac{R_{\text{strain}} - R_0}{\varepsilon}. \qquad (6)$$

This equation gives a GF of -41 for the core-shell device at 45-75% RH (inset of figure 10(c)). The large GF is due to the increase in the surface area of the flexible SnO_2 shell as the device is stretched. Since the response times of the device to the absorption and desorption of water molecules were almost the same regardless of the degree of strain (ε = 0 or 0.77%) (figure 10(a)), the chemical properties of the SnO_2 forming the shell were constant with or without strain. When the device was bent, the interstices and grain boundaries in the scaly structured shell expanded. Water molecules adsorbed on this surface and allowed current to flow through the nanostructured SnO_2, leading to a large change in the current and a large gauge factor when bending the device (figure 10(c)).

4. Flexible SnO_2 film sensors

SnO_2 is a gas sensing material that is widely used as a two-dimensional film sensor [35,36] rather than the wire sensor mentioned in this review, because SnO_2 films have a larger surface area, can adsorb more gases, and are easier to fabricate. The films can be fabricated on both solid substrates and flexible plastic films by vacuum deposition, electrochemical deposition, sputtering, laser ablation [37], or ink jet printing methods [38]. In addition, flexible SnO_2 films can be used as the *n*-type electron transparent layer (ETL) [39] of perovskite solar cells with n-i-p device architecture [40], because the SnO_2 material itself has excellent properties as an ETL material, including high light transmission with wide bandgap, high conductivity, high chemical stability, and the proper band energy alignment with perovskite layer. It is known that interfacial chemical engineering and interfacial modification

between the perovskite and SnO_2 layers play an important role in the practical application of efficient and stable n-i-p perovskite solar cells [41, 42]. As a solution to the interface problem, surface modification of SnO_2 with alkaline halide salts (e.g., KCl, KF, and RbF) [43, 44] and ammonium halide salts (e.g., NH_4Cl and NH_4F) [45, 46] and passivation of SnO_2 surface with functional organic compounds [46, 47] and SAM [48] have been applied and demonstrated their effectiveness [49]. Moreover, instead of SnO_2 films in the solar cells, SnO_2 and TiO_2 nanowire aggregates have been used as other candidates for ETL of the solar cells [50].

5. Summary

The present study demonstrates that novel functionalities can be created in rutile-structured SnO_2 microrods by applying mechanical stress and voltage and that β-Ga_2O_3/amorphous SnO_2 core/shell microribbons exhibit novel humidity sensitivity, which is enhanced by increasing the surface area of the SnO_2 through the application of mechanical stress. The design and fabrication of these hybridized oxide structures by nanoarchitectonics and the enhancement of the functionality by applying external stimuli pave the way for the creation of new functionalities. Since nano-/microrods with novel functionalities can be fabricated by appropriate material selection and their hybridized growth by nanoarchitectonics, the combination of these hybridized oxide wire aggregated layers with functional 2D materials will open a new avenue for the development of new 2D materials and sensors.

Acknowledgements

The author thanks Prof. Kewei Liu of CIOMP, Chinese Academy of Sciences, Prof. M. Aono of MANA, NIMS for fruitful discussion, and Dr. K. Terabe of MANA, NIMS for useful comments. This study is supported by WPI-MANA, MEXT, Japan and in part by JSPS KAKENHI (Grant number: 21K04821).

Notes

The author declares no competing financial support.

References

[1] Aono M, Bando Y and Ariga K 2012 Nanoarchitectonics: Pioneering a new paradigm for nanotechnology in materials development *Adv. Mat.* **24**, 150-151.

[2] Doherty R D, Hughes D A, Humphreys F J, Jonas J J, Jensen D J, Kassner M E, King W E, McNelley T R, McQueen H J and Rollett A D 1977 Current issues in recrystallization: a review *Mat. Sci. Eng. A* **238**, 219-274.

[3] Wu Y and Yang P 2001 Melting and welding semiconductor nanowires in nanotube *Adv. Mat.* **13**, 520-523.

[4] Sakthivel T S, Reid D L, Bhatta M, Möbus G, Sayle D C and Seal S 2015 Engineering of nanoscale defect patterns in CeO_2 nanorods via *ex site* and *in site* annealing *Nanoscale* **7**, 5169-5177.

[5] Yamazoe N 1991 New approaches for improving semiconductor gas sensors *Sens. Actuators B* **5**, 7-19.

[6] Wan Q, Dattolo E and Lu W 2008 Doping-dependent electrical characteristics of SnO_2 nanowires *Small* **4**, 451.

[7] Liu K W, Sakurai M and Aono M 2010 Indium-doped ZnO nanowires: Optical properties and room-temperature ferromagnetism *J. Appl. Phys.* **108**, 043516

[8] Liu K W, Sakurai M and Aono M 2012 Controlling semiconducting and insulating states of SnO_2 reversibly by stress and voltage *ACS Nano* **6**, 7209-7215.

[9] Göpel W and Schierbaum K D 1995 SnO_2 sensors; current status and future prospects *Sensors and Actuators B* **26-27**, 1 – 12.

[10] Das S and Jayaraman V 2014 SnO_2: A comprehensive review on structure gas sensors *Prog. Mat. Sci.* **66** 112-255.

[11] Ziman J M 1979 *Models of disorder* (Cambridge univ. press, Cambridge) Chap. 1.

[12] Sakurai M, Liu K W and Aono M 2014 Reversible and nonvolatile modulation of electrical resistance in SnO_2 by external strain *Appl. Phys. Express* **7**, 031101.

[13] Sakurai M, Liu K W and Aono M 2019 Reversible manipulation of lattice defects in single-crystal SnO_2 microrod by applying mechanical stress and voltage *J. Appl. Phys.* **125**, 082512.

[14] Liu K W, Sakurai M and Aono M 2012 One-step fabrication of β-Ga_2O_3-amorphous-SnO_2 core-shell microribbons and their thermally switchable humidity sensing properties *J Mat Chem* **22**, 12882-12887.

[15] Liu K W, Sakurai M and Aono M 2012 Enhancing the humidity sensitivity of Ga_2O_3/SnO_2 core/shell microribbon by applying mechanical strain and its application as a flexible strain sensor *Small* **8**, 3599-3604.

[16] Liu K W, Sakurai M and Aono M 2015 Ultrahigh-gain Single SnO_2 microrod photoconductor on flexible substrate with fast recovery speed *Adv. Func. Mat.* **25**, 3157-3163.

[17] Prades J D, Arbiol J, Cirera A, Morante J R, Avella M, Zanotti L, Comini E, Faglia G, Sberveglieri 2007 Defect study of SnO_2 nanostructures by cathodoluminescence analysis: Application to nanowire *Sensors and Actuators B* **126**, 6-12.

[18] Kar A, Kundu S and Patra A 2011 Surface defect-related luminescence properties of SnO_2 nanorods and nanoparticles *J. Phys. Chem. C* **115**, 118-124.

[19] Hartman T E, Blair J C and Bauer R 1966 Electrical conductance through SiO films *J. Appl. Phys.* **37**, 2468-2474.

[20] Ashbee K H G and Smallman 1963 The plastic deformation of titanium dioxide single crystals *Proc Roy. Soc. London, Ser. A* **274**, 195-205.

[21] Blanchin M G and Fontaine G 1975 Transmission electron microscope observation of deformed rutile (TiO_2) *Phys. Status Solidi A* **29**, 491-501.

[22] Liu Q, Bo A, Zhan H, Kou L, Gu Y, 2021 Reversible the mechanical bending mechanism of single-crystal rutile TiO_2 nanowires near room temperature: Implications for nanostructured semiconductor *ACS Appl. Nano. Mat.* **4**, 10354-10359.

[23] Zang J, Xu Z H, Webb R A, Li X 2011 Electrical self-healing of mechanically damaged zinc oxide nanobelts *Nano Lett.* **11**, 241-244.

[24] Razeghi M and Rogalski 1996 Semiconductor ultraviolet detectors *J. Appl. Phys.* **79**, 7433-7473.

[25] Hu L, Yan J, Liao M and Wu L 2011 Ultrahigh external quantum efficiency from thin SnO_2 nanowire ultraviolet photodetectors *Small* **7**, 1012-1017.

[26] Kim D, Shin G, Yoon J, Jang D, Lee S J, Zi G and Ha J S 2013 High performance stretchable UV sensor arrays of SnO_2 nanowires *Nanotechnology* **24**, 315502.

[27] Lu M L, Weng T M, Chen J Y and Chen Y F 2012 Ultrahigh-gain single SnO_2 nanowire photodetectors made with ferromagnetic nickel electrodes *NPG Asia Matter* **4**, e26.

[28] Dissanayake A, Elahi M, Jiang H X and Lin S J 1992 Kinetics of persistent photoconductivity in $Al_{0.3}Ga_{0.7}As$ and $Zn_{0.3}Cd_{0.7}Se$ semiconductor alloys *Phys. Rev. B* **45**, 13966-14004.

[29] Viana E R, Gonzalez J C, Ribeiro G M and Oliveira A G 2013 Photoluminescence and High-Temperature Persistent Photoconductivity Experiments in SnO_2 Nanobelts *J. Phys. Chem. C* **117**, 7844

[30] Kulwicki B M 1991 Humidity sensors *J. Am. Ceram. Soc.* **74**, 697-708.

[31] Traversa E 1995 Ceramic sensors for humidity detection: the state-of-the-art and future developments *Sensors and Actuators B* **23**, 135-156.

[32] Chen Z and Lu C 2005 Humidity sensors: a review of materials and mechanisms *Sens. Lett.* **3**, 274.

[33] Kuang Q, Lao C, Wang Z L, Xie Z and Zheng L 2007 High-Sensitivity Humidity Sensor Based on a Single SnO_2 Nanowire *J. Am. Chem. Soc.* **129**, 6070-6071.

[34] Morishige K, Kittaka S and Morimoto T 1981 Studies of two-dimensional condensation of water on hydroxylated ZnO, SnO_2, and Cr_2O_3: determination of two-dimensional critical temperature *Surf. Sci.* **109**, 291-300.

[35] Sberveglieri G 1995 Recent developments in semiconducting thin-film gas sensors, *Sensors and Actuators* **B 23**, 103-109.

[36] Göpel W, Schierbaum K D 1995 SnO_2 sensors: current status and future prospects, *Sensors and Actuators* **B 26-27**, 1 – 12.

[37] Nwanna E C, Imoisli P E and Jen T C 2020 Fabrication and synthesis of SnO_x thin films: a review, *The International Journal of Advanced Manufacturing Technology* **111**, 2809-2831.

[38] Shen W 2012 Properties of SnO_2 based gas-sensing thin films prepared by ink-jet printing, *Sensors and Actuators* **B 166-167**, 110-116.

[39] Jiang Q, Zhang X and You J 2018 SnO_2: a wonderful electron transport layer for perovskite solar cells, *small* **14**, 1801154.

[40] Kojima A, Teshima K, Shirai Y, Miyasama T 2009 Organometal halide perovskite as visible-light sensitizer for photovoltaic cells, *J. Am. Chem. Soc.* **131**, 6050-6051.

[41] Aydin E, Bastiani M D and Wolf S D 2019 Defect and contact passivation for perovskite solar cells, *Adv. Mater.* **31**, 1900428.

[42] Tong G, Ono L K, Liu Y, Zhang H, Bu T and Qi Y 2021 Up-scalable fabrication of SnO2 with multifunctional interface for high performance perovskite solar modules, *Nano-Micro Lett.* **13**, 155.

[43]

[44]

[45]

[46]

[47]

[48]

[49] Park S Y, Zhu K 2022 Advances in SnO_2 for efficient and stable n-i-p perovskite solar cells *Adv Mat* **34**, 2110438.

[50] Yeom E J, Shin S S, Yang W S, Lee S J, Yin W, Kim D, Noh J H, Ahn T K, Seok S I 2017 Controllable synthesis of single crystalline Sn-based oxides and their application in perovskite solar cell *J. Mat. Chem.* **A 5**, 79-86.